Computer Methods and Programs in Biomedicine 258 (2025) 108486

Contents lists available at ScienceDirect

Computer Methods and Programs in Biomedicine

journal homepage: https://www.sciencedirect.com/journal/computer-methods-and-programs-in-biomedicine

Computer model coupling hemodynamics and oxygen transport in the coronary capillary network: Pulsatile vs. non-pulsatile analysis

Haifeng Wang [a,*], Jenny S. Choy [b], Ghassan S. Kassab [b], Lik-Chuan Lee [a]

[a] Department of Mechanical Engineering, Michigan State University, East Lansing, MI, USA
[b] California Medical Innovations Institute, San Diego, CA, USA

ARTICLE INFO

Keywords:
Oxygen transport
Coronary capillary network
Capillary hemodynamics
Finite element modeling
Advection-diffusion
Oxygen consumption

ABSTRACT

Background and Objective: Oxygen transport in the heart is crucial, and its impairment can lead to pathological conditions such as hypoxia, ischemia, and heart failure. However, investigating oxygen transport in the heart using *in vivo* measurements is difficult due to the small size of the coronary capillaries and their deep embedding within the heart wall.
Methods: In this study, we developed a novel computational modeling framework that integrates a 0-D hemodynamic model with a 1-D mass transport model to simulate oxygen transport in/across the coronary capillary network.
Results: The model predictions agree with analytical solutions and experimental measurements. The framework is used to simulate the effects of pulsatile vs. non-pulsatile behavior of the capillary hemodynamics on oxygen-related metrics such as the myocardial oxygen consumption (MVO_2) and oxygen extraction ratio (OER). Compared to simulations that consider (physiological) pulsatile behaviors of the capillary hemodynamics, the OER is underestimated by less than 9% and the MVO_2 is overestimated by less than 5% when the pulsatile behaviors are ignored in the simulations. Statistical analyses show that model predictions of oxygen-related quantities and spatial distribution of oxygen without consideration of the pulsatile behaviors do not significantly differ from those that considered such behaviors (p-values > 0.05).
Conclusions: This finding provides the basis for reducing the model complexity by ignoring the pulsatility of coronary capillary hemodynamics in the computational framework without a substantial loss of accuracy when predicting oxygen-related metrics.

1. Introduction

Oxygen (O_2) transport in the heart is vital for cellular respiration and energy production, especially during exercise [1]. Efficient O_2 transport is essential for maintaining metabolic processes, while its impairment can lead to pathological conditions such as hypoxia, ischemia, and organ dysfunction. Impaired O_2 transport is also associated with heart failure arising from several etiologies such as diabetes and coronary artery diseases [1,2]. Advanced imaging techniques, such as positron emission tomography and computed tomography, can assess myocardial perfusion [3,4]. Investigation of dynamic O_2 transport in the heart from direct experimental measurements is, however, challenging because the capillaries are small and are largely embedded in the heart wall. Computational modeling can overcome this challenge by providing insights into the O_2 distribution and tissue oxygenation under different physiological, pathological and treatment conditions, which in turn, helps enhance our understanding of diseases and treatments mechanisms [5–8].

While several computer models of O_2 transport have been developed [6,7,9–12], they have some limitations. Specifically, the hemodynamics in some models are simplified, where nonlinearities associated with blood properties, such as viscosity, are disregarded [6,9,10]. In other studies, O_2 diffusion in the capillary is ignored [7] and simulations are restricted to a single capillary [11]. Most importantly, these studies have assumed steady-state hemodynamics [6,7,9–12], and none has considered whether capillary deformability and flow pulsatility affect O_2 transport in the capillary network and myocardial oxygen consumption (MVO_2). As pointed out by Beard and Bassingthwaighte [6], it is necessary to develop a generic modeling framework that can be used to consider O_2 transport under both steady-state and time-dependent conditions.

Accordingly, we have recently developed a computational model that integrates the coronary circulation of the entire coronary arterial–capillary–venous network in a closed-loop system [13]. The model has

* Corresponding author.
E-mail address: haifeng.wang@rub.de (H. Wang).

https://doi.org/10.1016/j.cmpb.2024.108486
Received 20 August 2024; Received in revised form 1 October 2024; Accepted 30 October 2024
Available online 8 November 2024

been validated and applied to myocardial ischemia and therapeutic interventions such as coronary sinus reducer [14] and preconditioning with selective autoretroperfusion [15]. The model, however, does not consider O_2 transport, which is essential for understanding myocardial metabolism and function. Similarly, other recent studies that couple coronary arterial flow with myocardial perfusion [16–18] also did not consider oxygen transport. Motivated by these issues, we seek here to develop a computational framework that couples the hemodynamics model as described in [13] with the transport of O_2 in/across the capillary network and the consumption of O_2 by the myocardial tissues. The coupled hemodynamics-O_2 transport computational framework is then applied to investigate the effects of flow pulsatility and key physiological parameters on O_2 transport dynamics in/across the coronary capillary network.

2. Methods

This computational modeling framework couples a 0-D nonlinear lumped-parameter flow model that considers hemodynamics [13] with a 1-D finite element model of O_2 transport in the coronary capillary network. In this framework, vessel diameters and flow rates computed from the 0-D flow solver are applied to the 1-D O_2 transport solver (Fig. 1). As described in details below, the O_2 transport solver considers five processes in and across two principal domains (intravascular and extravascular). These processes are, namely, (1) Advection and (2) Diffusion of both free and hemoglobin-bound O_2 within each vessel, (3) Permeation (diffusion) of free O_2 across the capillary walls, (4) Diffusion of myoglobin-bound O_2 within the surrounding tissues, and (5) O_2 consumption by the tissue.

2.1. Blood flow

To predict flow rates and vessel diameters in a capillary network, we use a 0-D nonlinear lumped-parameter model that has been developed and validated [13]. Briefly, each vessel i of the capillary network is represented by a lumped model consisting of two dynamically-varying resistances $R^i_{1,2}$ and a capacitance C^i (as indicated in Fig. 1). Analogous to Ohm's law, the flow rate of vessel i, Q_i, is given by:

$$Q_i = \frac{P^i_{\text{in}} - P^i_{\text{out}}}{R^i_1 + R^i_2}. \tag{1}$$

Mass conservation in vessel i requires:

$$\frac{P^i_{\text{in}} - P^i_{\text{mid}}}{R^i_1} + \frac{P^i_{\text{out}} - P^i_{\text{mid}}}{R^i_2} = C^i \left(\frac{d(P^i_T - P^i_{\text{mid}})}{dt} \right), \tag{2}$$

where P^i_{in} and P^i_{out} are the inlet and outlet pressures; P^i_{mid} and P^i_T are the intravascular and extravascular pressures, respectively, with the latter being the intramyocardial pressure (IMP). The two resistances $R^i_{1,2}$ are assumed to be identical and are determined by:

$$R^i_1(t) = R^i_2(t) = \frac{64\mu^i(t)L^i}{\pi(D^i(t))^4}, \tag{3}$$

where L and D are the length and diameter of the vessel, respectively; μ is the blood viscosity and is prescribed as:

$$\mu = \left[1 + \left(6e^{-0.085D} + 3.2 - 2.44e^{-0.06D^{0.645}} \right) \left(\frac{D}{D-1.1} \right)^2 \right] \left(\frac{D}{D-1.1} \right)^2. \tag{4}$$

The capacitance is given by:

$$C^i(t) = \frac{\partial \left(\pi(D^i(t))^2 L^i/4 \right)}{\partial \left(P^i_{\text{mid}}(t) - P^i_T(t) \right)}. \tag{5}$$

Both $R^i_{1,2}$ and C^i depend on the diameter D^i, which in turn depends on the trans-vascular pressure, $\Delta P = P^i_{\text{mid}} - P^i_T$, as:

$$D(\Delta P) = 2B_p + \frac{2(A_p - B_p)}{\pi} \left[\frac{\pi}{2} + \arctan\left(\frac{\Delta P - \psi_p}{C_p} \right) \right], \tag{6}$$

where A_p and B_p are the asymptotical highest and lowest radii, respectively; ψ_p is the transvascular pressure corresponding to the mean of radii A_p and B_p, while C_p is the passive response bandwidth. These passive vessel parameters are obtained by fitting Eq. (6) to experimental data [19]. The capillary network is described by a system of nonlinear ordinary differential equations (ODEs) obtained by invoking mass conservations in each vessel. Generalized formulations describing the coronary system are provided in the Appendix (Generalized network formulation).

2.2. Advection, diffusion and permeation of O_2 in the blood

The transport equations governing intra-vascular advection and diffusion, as well as trans-capillary permeation, are formulated as [5–7,10,20]:

$$\frac{dC_T(x,t)}{dt} = -U\frac{dC_T(x,t)}{dx} + D_F\frac{d^2C_F(x,t)}{dx^2} + D_{Hb}\frac{d^2C_B(x,t)}{dx^2} - \frac{\kappa_w A}{V_b}(C_F - C^t_F), \tag{7}$$

where $U(x,t)$ is the flow velocity; V_b is the blood volume and A is the vascular wall surface area that are both determined from the vessel diameter and length; κ_w is the vessel wall permeability; D_F is the free O_2 diffusion coefficient with a typical value of $2.41 \times 10^{-5}\,\text{cm}^2/\text{s}$ [6] whereas D_{Hb} is the hemoglobin diffusion coefficient that is lower than D_F as hemoglobin molecules diffuse approximately 65 times slower than free O_2 molecules [5].[1]

In Eq. (7), $C_T(x,t)$ is the total O_2 concentration at position x and time t. The total O_2 concentration is the sum of the free and bound O_2 concentration, i.e., $C_T = C_F + C_B$, where C_F is the free O_2 concentration and C_B is the bound O_2 concentration. In the vasculature, typically less than 2% of the total O_2 is dissolved in plasma. The vast majority (about 98.5%) of the O_2 is bounded to hemoglobin, a protein in red blood cells (RBCs). The free O_2 concentration in tissues surrounding the blood vessel is denoted as C^t_F. Both free O_2 concentrations C_F and C^t_F, are expressed in the unit of moles per liter of blood (mol/L) in Eq. (7) and can be easily converted to the partial pressure of oxygen (pO_2) using the relationship $pO_2 = C_F/\alpha$, where the solubility coefficient $\alpha = 1.35 \times 10^{-6}\,\text{M/mmHg}$.[2] We note that pO_2 specifically measures the pressure exerted by free O_2 dissolved in either the blood plasma or

[1] In principle, the diffusion term $D_F\frac{d^2C_F(x,t)}{dx^2} + D_{Hb}\frac{d^2C_B(x,t)}{dx^2}$ in Eq. (7) can be simplified and represented by a single term as $D_{\text{eff}}\frac{d^2C_T(x,t)}{dx^2}$, where D_{eff} denotes the effective O_2 diffusion coefficient [5,21]. The parameter D_{eff} controls the combined diffusion of both free O_2 in plasma and O_2 bound to hemoglobin, which simplifies the computational model by encapsulating the net effect of O_2 transport through both mechanisms. The parameter D_{eff} is, however, not well estimated. Therefore, the application of D_{eff} must be carefully calibrated and validated against experimental data to ensure its physiological relevance and accuracy. In comparison, both the diffusion coefficient for free O_2 in plasma and oxyhemoglobin, which is the form of hemoglobin bound to O_2, are better estimated [5].

[2] This conversion uses the relationship between the free O_2 concentration and the solubility coefficient (denoted as α), according to Henry's law. The value of the α is determined based on the well-known measurement of approximately 0.003 mL/mmHg of O_2 per dL of blood (1 dL = 100 mL). Specifically, at standard temperature and pressure, 1 mole of any ideal gas (e.g., O_2) occupies 22.4 liters, i.e., 1 mol = 22,400 mL. Therefore, $\alpha = 1.35 \times 10^{-6}$ M/mmHg can be converted to approximately 0.003 mL/mmHg of O_2 per 100 mL of blood, indicating that approximately 0.3 mL O_2 dissolved in 100 mL blood when the blood pO_2 is 100 mmHg.

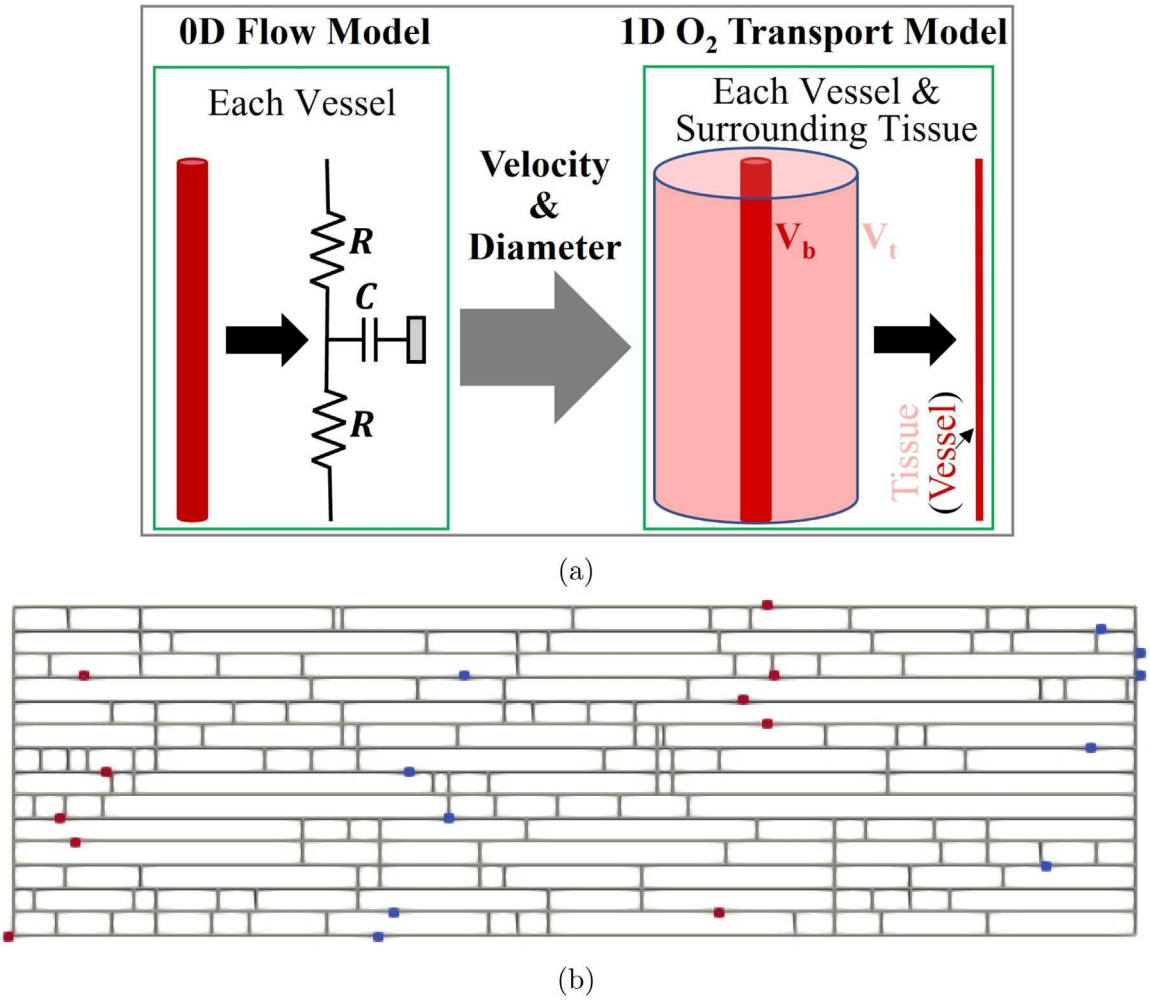

Fig. 1. Schematic of the hybrid 0D-1D computational framework (top panel). Flow dynamics and vessel deformation are accounted for using a 0-D nonlinear lumped parameter model, where each vessel segment is represented by a three-element Windkessel model, comprising of two resistances (R) and a capacitance (C). O_2 transport is simulated using a 1-D finite element approach that models both the vessel and its surrounding tissue as line entities (overlaid), inspired by the Krogh-cylinder model. V_t is the tissue volume associated with the capillary vessel of blood volume V_b. A capillary network is generated based on experimental data by randomly placing 10 arterioles (red dots) and 10 venules (blue dots) within a two-dimensional domain (bottom panel).

the tissues, and is a common metric used in experimental and clinical reports. In this study, unless otherwise specified, we impose a pulsating pO_2 with a mean value of 95 mmHg at the inlets [22,23] and a no-flux boundary condition at the outlet cross-sections. The pO_2 at the outlets of the simulated system is allowed to vary and changes dynamically throughout the simulation.

The bound O_2 concentration depends on C_F by:

$$C_B = 4C_{Hb}H_{ct}S_{Hb}(C_F), \tag{8}$$

where C_{Hb} is the hemoglobin concentration in the RBCs, H_{ct} is the hematocrit, and S_{Hb} is the O_2 saturation of hemoglobin. The value of C_{Hb} is typically measured in terms of the mean corpuscular hemoglobin concentration (MCHC), which is the average concentration of hemoglobin in a given volume of packed RBCs. The normal range for MCHC in humans is approximately 34 ± 2 g/dL [24]. When taken together with the molar mass of hemoglobin in adult human hemoglobin at approximately 64,500 grams per mole (g/mol), $C_{Hb} \approx 5.3 \times 10^{-3}$ M. The capillary hematocrit is generally lower than the systemic hematocrit as well as the arterial hematocrit. While the systemic hematocrit in adult humans is generally in the range of 35–50% [25], the effective H_{ct} in capillaries can vary between 15% to 35% [20,26,27]. The O_2 saturation of hemoglobin S_{Hb} is governed by the Adair equation [28]:

$$S_{Hb}(C_F) = \frac{aX^n + bX^{2n}}{1 + cX^n + bX^{2n}}, \tag{9}$$

where $X = \frac{C_F/\alpha}{P_{50}} 10^{0.024(37-T_{\text{temp}})+0.4(pH-7.4)+0.06\log(40/pCO_2)}$ [28]. The fitted parameters, denoted as a, b, c, and n, are 0.34332, 0.64073, 0.34128, and 1.58678, respectively [28]. The temperature T_{temp}, partial pressure of CO_2 (pCO_2), pH value and half-saturation pressure of hemoglobin P_{50} are set at 37 °C, 40 mmHg, 7.4, 26.8 mmHg [20], respectively.

2.3. Permeation, consumption and diffusion of O_2 in the tissue

In this model, we assume that any O_2 crossing the vessel wall disperses uniformly across the tissue volume perpendicular to the vessel axis as assumed in [7]. We also consider the diffusion within the surrounding tissues in the direction parallel to the vessel axis to avoid unrealistic sharp change in the O_2 content (as indicated in Fig. D.1). Similar to [6,10], we ignore the interstitial space and do not consider any potential advection within the extravascular regions. The surrounding finite tissue volume of a capillary is modeled as a 1-D line (Fig. 1). Correspondingly, the equation for regional permeation and consumption (chemical reactions) as well as diffusion of O_2 in the tissue

is given by:

$$\frac{dC_F^t(x,t)}{dt} = \frac{\kappa_w A}{V_t}(C_F - C_F^t) - \mathrm{MVO}_2(C_F^t) + D_F^t \frac{d^2 C_F^t}{dx^2} + D_{Mb} C_{Mb} \frac{d^2 S_{Mb}}{dx^2}, \tag{10}$$

where the last two terms describe the diffusion of free O_2 and O_2 binding to the tissue myoglobin [6,7,10,20]. The tissue free O_2 diffusion coefficient, D_F^t, is the same as that in blood (i.e., $D_F^t = D_F = 2.41 \times 10^{-5}\,\mathrm{cm}^2/\mathrm{s}$). The myoglobin diffusion coefficient D_{Mb} is taken to be $D_F^t/110$ [6]. The tissue myoglobin concentration $C_{Mb} = 1 \times 10^{-4}$ M. The binding of O_2 to myoglobin is governed by the two-state equilibrium expression [6]:

$$S_{Mb}(C_F^t) = \frac{C_F^t}{C_F^t + C_{50}}, \tag{11}$$

where C_{50} is the free O_2 concentration at 50% saturation that has a value of 2.5 Torr (1 Torr ≈ 1 mmHg). In Eq. (10), V_t is the tissue volume associated with the capillary vessel. The ratio of capillary blood volume to myocardial tissue volume, V_b/V_t, also known as capillary volume fraction or capillary volume density, is an important morphometric parameter and can vary inter- and intra-species. The ratio of coronary artery volume to myocardial volume is reported to be approximately 2.52% (min: 0.56%; max: 6.25%) in human hearts [29]. The ratio of capillary volume would reasonably be expected to be higher than that of large coronary arteries due to the dense network of capillaries in the myocardium. In this study, we prescribed $V_b/V_t = 8\%$ based on measurements showing that there are approximately 0.75 capillaries for every muscle fiber in the left ventricle (0.65 capillary for every myofiber in the right ventricle) of rats [30] and approximately 1 capillary for every muscle fiber in humans and dogs [31]. We note that the diameters of a healthy adult cardiomyocyte and coronary capillary are typically 10–25 μm [32–35] and 5–8 μm [36], respectively.

The rate of O_2 consumption MVO_2 in Eq. (10) is a function of the free O_2 concentrations in the tissue and can be modeled based on Michaelis–Menten enzyme kinetics [6] by:

$$\mathrm{MVO}_2(C_F^t) = \frac{G_{max} C_F^t}{C_F^t + K_m}, \tag{12}$$

where G_{max} is the maximum rate of O_2 consumption and represents the maximal capacity of the tissue to consume O_2 when O_2 availability is not a limiting factor. The parameter G_{max} serves as a reflection of the tissue's maximum metabolic needs. In healthy humans, MVO_2 of the entire heart is estimated to be approximately 25.2 mL/min [37], which is equivalent to 65.625 μM/s.[3] In this study, we prescribed $G_{max} = 70$ μM/s for the control/normal case. In Eq. (12), K_m is the apparent Michaelis constant for O_2 conversion by cytochrome oxidase, which reflects the O_2 affinity of cytochrome oxidase (the affinity of the cellular respiration machinery for O_2). A smaller K_m indicates a higher affinity of the tissue for O_2 that produces a higher reaction rate. In the myocardial tissue, the affinity of mitochondrial enzymes for O_2 is high, which ensures that aerobic metabolism in the heart is maintained even when O_2 levels are relatively low. Correspondingly, we prescribed $K_m = 0.1$ μM based on a previous study [6]. The relationship between S_{Hb} and blood pO_2, as well as between MVO_2 and tissue pO_2, is illustrated in Fig. D.2.

2.4. Oxygen metrics

The oxygen extraction ratio (OER) is defined as the fraction of O_2 removed from the blood during its passage through the capillaries, and is commonly calculated based on the difference between oxygen content of arterial blood and oxygen content of venous blood, i.e.:

$$\mathrm{OER} = \frac{\mathrm{CaO}_2 - \mathrm{CvO}_2}{\mathrm{CaO}_2} \times 100, \tag{13}$$

where CaO_2 is the pre-capillary arteriolar O_2 content and CvO_2 is the post-capillary venular O_2 content. The unit commonly used for CaO_2 and CvO_2 is milliliters of O_2 per deciliter of blood (denoted as 'mL O_2/dL blood', i.e., 'mL O_2/100 mL blood'), reflecting the volume of oxygen carried in 100 mL blood. The post-capillary venular O_2 content CvO_2 includes both the O_2 bound to hemoglobin and the free O_2 dissolved in plasma at the cross-sectional area A_c of all outlets, and can be calculated by:

$$\mathrm{CvO}_2 = \frac{1}{T}\int_{t_0}^{t_0+T} \frac{1}{A_c^{\mathrm{out}} \cdot \delta x} \int_{x_{\mathrm{out}}}^{x_{\mathrm{out}}+\delta x} A_c(x,t) \cdot \left(C_F(x,t) + C_B(x,t)\right)\, dx\, dt, \tag{14}$$

where A_c^{out} represents the total cross-sectional area of all outlets; $A_c(x,t)$ denotes the cross-sectional area at position x and time t; T denotes the timespan associated with the analysis, such as the period of a single breathing or cardiac cycle; δx is a very short axial distance over which the concentration of oxygen can be reasonably assumed to be constant and uniform. The term δx is introduced to simplify the understanding of the mathematical definition of CvO_2. The purpose of the factor $1/A_c^o \delta x$ can be understood by considering two outlets with O_2 contents of 1 mol O_2/1 mL blood and 3 mol O_2/1 mL blood, respectively. Accordingly, the CvO_2 should be 1.5 mol O_2/1 mL blood (or equivalently 3 mol O_2/2 mL blood), rather than 2 mol O_2/1 mL blood. The pre-capillary arteriolar O_2 content CaO_2 is computed in the same way using C_F and C_B at the inlets. Both C_F and C_B obtained through Eq. (7) are expressed in mol/mL (or mol O_2/1 mL blood[4]), reflecting the amount of O_2 carried in 1 mL blood.

The rate of tissue oxygen extraction (OE) for a given tissue volume (V_t) is calculated by:

$$\mathrm{OE} = \frac{1}{T}\int_{t_0}^{t_0+T} \frac{1}{V_t} \int_{x}^{x+L} \pi D(x,t) \cdot \kappa_w \left(C_F(x,t) - C_F^t(x,t)\right)\, dx\, dt, \tag{15}$$

where D and L are the vessel diameter and length, respectively. The OE computed from Eq. (15) is expressed in 'mol O_2/s/1 mL tissue'.[5] At the steady-state, the OE is identical to the rate of oxygen consumption by the myocardium, i.e., MVO_2 (Eq. (12)).

2.5. Capillary network

We consider six capillary networks (Figs. 1b and D.3) generated based on previous studies [13,36]. The representative (baseline) network shown in Fig. 1b consists of 10 arterioles, 10 venules, and 729 capillaries. The branching ratio between capillaries and arterioles or venules is 3. To examine the effect of the network structure on oxygen-related metrics, we also considered five additional networks (Fig. D.3) that differ in the branching ratio between capillaries and arterioles/venules, as well as in capillary cross-connections within experimental measurements [36]. In all networks, the distribution of arterioles and venules is generated pseudo-randomly based on the mean

[3] by a factor of 2.6, given that 1 mol = 22,400 mL, the typical human heart weighs 300 g with a density of 1.05 g/mL, and 1 μM = 1×10^{-9} mol/mL.

[4] The unit of 'mol O_2/mL blood' can be directly converted to 'mL O_2/dL blood' by a factor of 2,240,000. Note that a hematocrit value of 0.25 ($H_{ct} = 0.25$) is used in the calculations for pre-capillary CaO_2 and post-capillary CvO_2. These values are expected to be lower than the arterial O_2 content found in larger vessels, which typically have a hematocrit of 0.45. We note that the normal arterial O_2 content is approximately 20 mL O_2/dL blood in larger vessels in a healthy person.

[5] This unit can be directly converted to the more commonly used unit of 'mL O_2/min/100 mL tissue' by a factor of 134,400,000 (note that 1 mol/s = 1,344,000 mL/min).

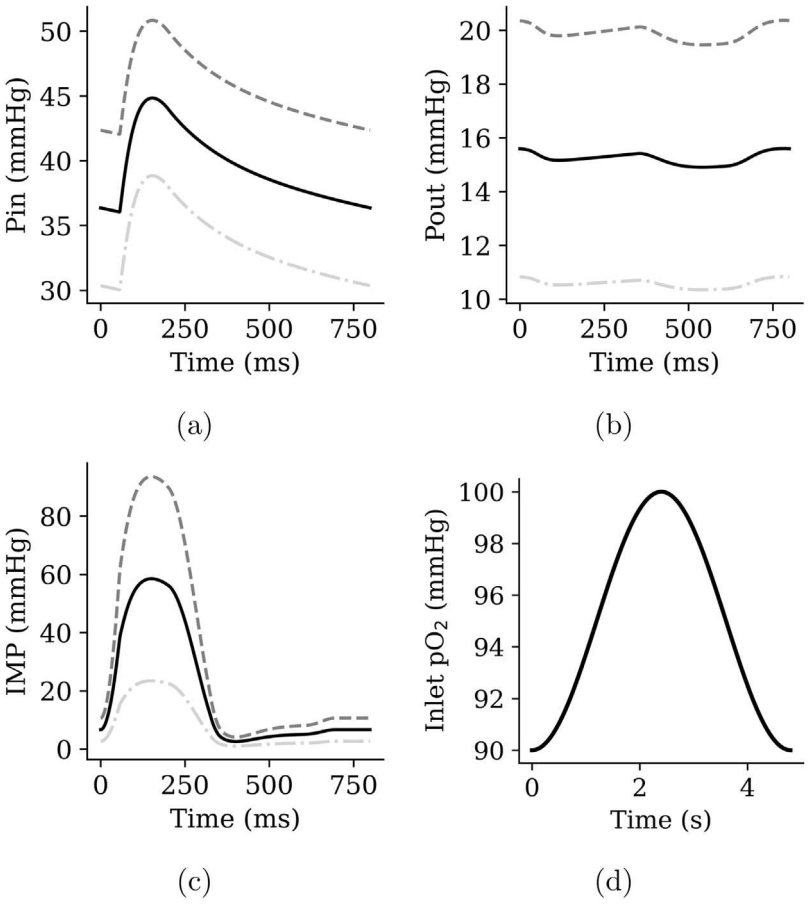

Fig. 2. Boundary Conditions. Pulsatile waveforms of (a) inlet pressure (P_{in}), (b) outlet pressure (P_{out}), and (c) intra-myocardial pressure (IMP) within a cardiac cycle applied at the inlets and outlets as well as at each vessel wall of the capillary network. These pressure waveforms and their mean values are based on previous studies [13,25,38]. (d) Waveform of pO_2 within a respiratory cycle based on [23,39] is prescribed at all inlets (arterioles) of the network. Different combinations of pulsatile P_{in}, P_{out} and IMP result in a total of 27 "pulsatile" simulations, each with varying inlet, outlet, and intra-myocardial pressures. Dashed and dash-dotted lines in (a) and (b) represent waveforms with different mean pressures. Dashed line in (c) corresponds to waveform associated with the endocardial IMP, while the dash-dotted line corresponds to waveform associated with the epicardial IMP.

functional capillary lengths (i.e., linear distance between the centers of mass of adjacent arteriolar and venular domains) measured in pigs, which is 510 ± 178 μm in the right ventricle and 512 ± 163 μm in the left ventricle [36]. The average distance between an arteriole source and its closest venule sink is approximately 510 ± 170 μm for all networks considered (Figs. 1b and D.3).

2.6. Simulation cases

The computational model was first verified against the analytical solutions found in a single vessel. Sensitivity analyses were subsequently performed on the capillary network (Fig. 1) to understand the effects of key model parameters. Simulations of O_2 transport were also performed on the capillary network to investigate changes in oxygen-related metrics under pulsatile and non-pulsatile perfusion.

2.6.1. Single vessel numerical solution verification

Simulations of (1) O_2 *'advection + diffusion'* in a single capillary vessel and (2) O_2 *permeation* across a single capillary vessel wall were performed and their results were verified with analytical solutions. For these simulations, the capillary vessel has a diameter of $D = 6$ μm and a length of $L = 1000$ μm (vessel surface area $A = \pi DL$; vessel cross-sectional area $A_c = \pi D^2/4$; vessel volume $V_b = A_c L$).

In the verification simulation of O_2 *'advection + diffusion'* in a single capillary vessel, the vessel wall permeability is set to zero, i.e., $\kappa_w = 0$ (i.e., no permeation). The oxygen diffusion coefficient D_F is set to 2.41×10^{-5} cm^2/s and we consider only free oxygen, i.e., $C_B = 0$ and $C_T = C_F$. A Gaussian-hill-type concentration was introduced at $l = 0.3$ mm. We consider advection-dominated transport where the flow rate in the vessel is $Q = 1.5 \times 10^{-3}$ mm^3/s (velocity $U = Q/A_c$) (Fig. 3a; Peclet number Pe = 110) and diffusion-dominated transport where $Q = 1.5 \times 10^{-6}$ mm^3/s (Fig. 3b; Pe = 0.11).

In the verification simulation of O_2 *permeation* across a single capillary vessel wall, we set $\kappa_w = 35$ μm/s, $U = 0$, $D_F = D_{Hb} = 0$, $G_{max} = 0$, and $V_t = V_b$. Initial blood pO_2 was set to 95 mmHg and tissue pO_2 was set to 0 mmHg.

2.6.2. Sensitivity analyses

To better understand the model, steady-state simulations were performed on the capillary network (Fig. 1) to analyze how pO_2 and oxygen-related metrics change with key model parameters. The sensitivity analyses were performed with respect to the baseline values shown in Table 1. In these analyses, we vary the maximum rate of O_2 consumption G_{max}, ratio of capillary blood volume to myocardial tissue volume V_b/V_t, capillary permeability κ_w, blood flow rate Q, and vessel diameter D by a factor of 0.5, 0.75, 1.25, and 1.5 with respect to their corresponding baseline values. We also vary H_{ct} by a factor of 0.4, 0.8, 1.2, and 1.8 with respect to the baseline values. The inlet (arterioles) partial pressure of oxygen pO_2 is prescribed to be 95 mmHg in these simulations.

Table 1
Baseline values of the hematocrit H_{ct}, maximum rate of oxygen consumption G_{max}, vascular volume fraction V_b/V_t, permeability κ_w, average flow rate Q_{mean}, and average diameter D_{mean}. Q_{mean} and D_{mean} are computed over all capillaries in the network (Fig. 1), where the constant inlet, outlet, and intra-myocardial pressures at the inlets, outlets, and vessel walls are set at 40 mmHg, 20 mmHg, and 20 mmHg, respectively.

H_{ct} (%)	G_{max} (μM/s)	V_b/V_t (%)	κ_w (μm/s)	Q_{mean} (mL^3/s)	D_{mean} (μm)
25	70	8	35	4.1×10^{-9}	5.9

2.6.3. Simulations of nonpulsatile and pulsatile perfusion

Simulations with pulsatile and non-pulsatile perfusion were performed to compare their predictions of oxygen-related metrics. In total, 27 simulations with varying inlet, outlet, and intra-myocardial pressures based on pulsatile pressure waveforms (Fig. 2) from previous studies [13,25,38] were performed on the capillary network (Fig. 1). Temporal variation of O_2 concentration is also considered where the waveform shown in Fig. 2d based on [23,39] is applied at all inlets of the network for each "pulsatile" simulation. We note the significant difference between respiratory rates (12 to 20 bpm) and heart rates (60 to 100 bpm), where some studies have shown that the temporal variation of arterial pO_2 follows the respiratory cycle [23,39]. For each "pulsatile" simulation, the mean value of the pressure waveforms over a cardiac cycle and the mean value of pO_2 over a respiratory cycle are used in the corresponding "non-pulsatile" simulation. Baseline values of H_{ct}, G_{max}, V_b/V_t, and κ_w shown in Table 1 were used in all the simulations here.

3. Results

3.1. Verification of the numerical solution

Fig. 3 shows the comparison between numerical and analytical solutions of the dynamic change in pO_2 over time under different conditions, namely, (1) advection-dominated transport (Peclet number Pe = 110), (2) diffusion-dominated transport (Pe = 0.11), and (3) O_2 permeation across a single vessel wall. The differences between the numerical and analytical solutions of advection dominated (Fig. 3a), diffusion dominated (Fig. 3b) and permeation O_2 transport (Fig. 3c) are all less than 1%. Details of the analytical solutions are given in Analytical Solutions for Benchmark Tests. In the figure, an increase in flow rate by a factor of 1000 (Fig. 3a), where Pe = 110, causes the pO_2 concentration waveform to travel 1000 times faster compared to that when Pe = 0.11 (Fig. 3b). On the other hand, higher permeability results in the blood and tissue pO_2 equilibrating earlier downstream (Fig. 3c).

3.2. Sensitivity analyses

Fig. 4 shows the effects of H_{ct}, V_b/V_t, Q, D, G_{max}, and κ_w on the OER, MVO_2 (i.e., tissue O_2 extraction rate), blood pO_2, and tissue pO_2. At baseline, the OER is 66%, MVO_2 is identical to tissue O_2 extraction rate and equal to 8.2 mL O_2/min/100 mL tissue, blood pO_2 is 32 ± 12 mmHg, and tissue pO_2 is 11 ± 10 mmHg.

With increasing hematocrit H_{ct}, MVO_2, tissue and blood pO_2 are all increased while OER is reduced (Fig. 4a). The increase in MVO_2 with H_{ct} is nonlinear, where the increase is larger at low H_{ct} before reaching saturation at approximately 12% higher than the baseline when H_{ct} = 0.45. The effects of vascular volume fraction V_b/V_t and flow rate Q on the O_2 quantities (Fig. 4b,c) are similar to that with H_{ct}. Similarly, MVO_2 becomes saturated at 115% and 110% of the baseline value as V_b/V_t and Q are increased, respectively. At the highest level of V_b/V_t and Q, tissue pO_2 is 395% and 170% of the baseline value, blood pO_2 is 139% and 123% of the baseline value, and OER is 56% and 72% of the baseline value. Increasing vessel diameter D results in opposite changes with respect to the parameters H_{ct}, V_b/V_t and Q (Fig. 4d). Specifically, MVO_2, tissue and blood pO_2 are all decreased while OER is increased with increasing D. Increasing maximum O_2 consumption rate G_{max} and capillary wall permeability κ_w affects OER and MVO_2 similarly (Fig. 4e,f). Specifically, as G_{max} and κ_w are increased, both OER and MVO_2 saturate at approximately 110% and 108% of their baseline values, respectively. Unlike H_{ct}, V_b/V_t and Q, the blood pO_2 is reduced with increasing G_{max} and κ_w. Tissue pO_2 level is increased (by 63% at the highest level) with κ_w, but is reduced (by 86% at the highest level) with G_{max}. The pre-capillary O_2 content remains stable across these parameter changes, except when adjusting H_{ct}. Increasing H_{ct} from 0.1 to 0.45 linearly raises the pre-capillary O_2 from 5 mL O_2/dL blood to 21 mL O_2/dL blood.

3.3. Comparison between non-pulsatile and pulsatile perfusion

Fig. 5 shows the predicted spatial distribution of pO_2 in the blood and tissue associated with the capillary network under both pulsatile and non-pulsatile perfusion. The mean inlet, outlet, and intra-myocardial pressures applied to the capillary network are 40 mmHg, 20 mmHg, and 20 mmHg, respectively. There is no significant difference in the spatial distribution of pO_2 in the blood and tissue of the capillary network between the pulsatile and non-pulsatile perfusion cases.

Fig. 6 shows the comparisons of the predicted oxygen-related metrics between the pulsatile and non-pulsatile perfusion simulation cases. In the pulsatile group, OER is $67 \pm 15.1\%$, post-capillary O_2 content is 3.9 ± 1.8 mL O_2/dL blood, MVO_2 is 7.8 ± 1.1 mL O_2/min/100 mL tissue, post-capillary pO_2 is 19.5 ± 6.4 mmHg, tissue pO_2 is 10.1 ± 3.9 mmHg, time-average flow rate over a cardiac cycle is $4.5 \pm 1.2 \times 10^9$ mL/s, and time-average capillary diameter is 5.9 ± 0.1 μm.

Compared to the pulsatile simulations, post-capillary O_2 content, MVO_2, post-capillary venous pO_2, tissue pO_2, time-averaged flow rate and vessel diameter are 17.5%, 4.4%, 13.2%, 19%, 3.6% and 0.02% higher in the non-pulsatile simulations, respectively. The average OER over all cases is 8.6% smaller in the non-pulsatile group. A two-tailed t-test shows that there is no significant difference between these two groups. Specifically, the lowest p-value is 0.12 in the model prediction of post-capillary venous pO_2.

Fig. D.3 shows the predicted spatial distribution of blood pO_2 in five additional capillary networks under pulsatile and non-pulsatile perfusion conditions. No significant differences were observed in the blood pO_2 distribution between the two perfusion types. For each vascular network, the spatial distribution of tissue pO_2 exhibits similar patterns under both conditions, as illustrated in the representative case shown in Fig. 5.

Fig. D.5 compares the predicted oxygen-related metrics between pulsatile and non-pulsatile perfusion groups, each consisting of six different capillary networks (Figs. 5 and D.3). The mean and standard deviation were calculated for both perfusion types across all networks. A two-tailed t-test revealed no significant differences between the pulsatile and non-pulsatile perfusion cases across all capillary networks considered (p-values > 0.05). Over all simulations (32 simulations for each of the pulsatile and non-pulsatile perfusion groups; Figs. 6 and D.5), the lowest p-value is 0.1 in the model prediction of post-capillary pO_2 (Fig. D.6).

Fig. D.7 shows that the pulsatile amplitude of pre-capillary O_2 concentration and its phase difference relative to the cardiac cycle do not significantly influence the model's predictions of O_2-related metrics. Furthermore, the mean amplitude of pO_2 across the capillary network is approximately 2.5% of the inlet pO_2 (SD = 8.6%; Table 2).

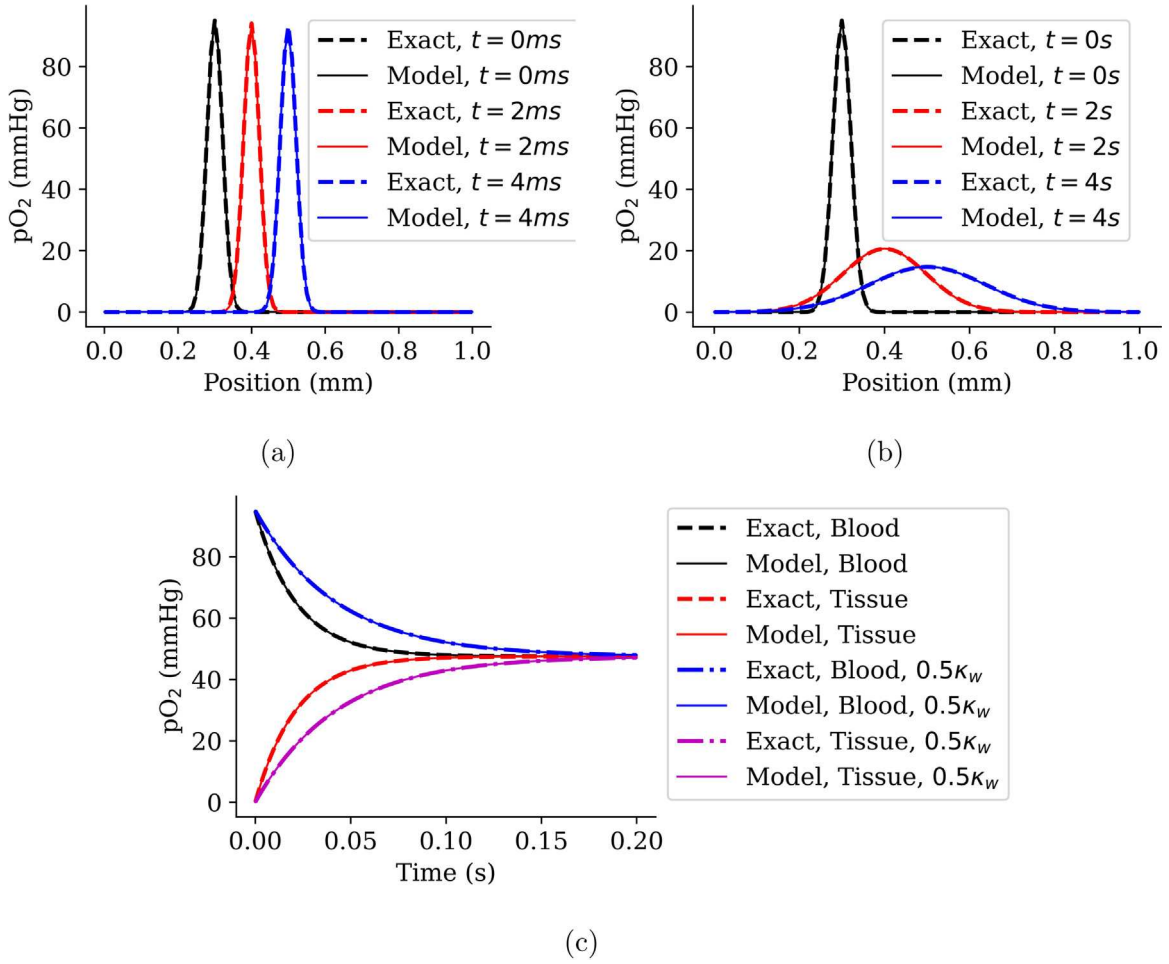

Fig. 3. Validations. Comparison of single-vessel numerical and analytical solution of (a) pO_2 profiles along the vessel for advection-dominated transport (Peclet number Pe = 110). (b) pO_2 profiles along the vessel for diffusion-dominated transport (Pe = 0.11). (c) Blood and tissue pO_2 evolutions over time towards equilibrium under two different levels of permeability: $\kappa_w^* = \kappa_w$ vs. $\kappa_w^* = 0.5\kappa_w$ where $\kappa_w = 35\,\mu m/s$. In simulations shown in panels (b) and (c), the finite element size is $\Delta L = 0.01L$ and the time step size $\Delta t = 0.02\,s$. In simulations shown in panel (a) where $Pe = 110$ as the flow rate is increased by a factor of 1000, the time step size is decreased by a factor of 1000 (CFL = 0.1) to avoid numerical instability (larger CFL, particularly CFL > 0.5 caused non-negligible numerical errors as indicated in Fig. D.4). The pO_2 is related to the oxygen concentration, C, and the solubility coefficient of oxygen, α, by $pO_2 = C/\alpha$.

Table 2
Comparison of O_2 amplitude between pre-capillaries (inlets) and capillaries in the network, indicating the impact of inlet O_2 on O_2 pulsatility within the capillary network. Input waveforms are shown in Fig. 2. The mean pressures at the inlets, outlets, and vessel walls are 40 mmHg, 20 mmHg, and 20 mmHg, respectively. The inlet pO_2 amplitude (Fig. 2d) was modified between 10 mmHg and 30 mmHg.

	Pulsatile O_2 Amplitude (mmHg)		
Pre-capillary	10	20	30
Capillaries	0.24 ± 0.86	0.5 ± 1.69	0.74 ± 2.58

4. Discussion

A major finding of our study is that the model predictions of O_2-related quantities without consideration of the pulsatile hemodynamics and pO_2 do not differ much from those obtained when the pulsatile behavior of these quantities is considered (with p-values > 0.05 in statistical analyses; Figs. 6, D.5 and D.6). The simulations also show that the spatial distribution of O_2 is insensitive to the pulsatile effects of the capillary flow and pressure (diameter) (Fig. 5). The insensitivity of the model predictions to the pulsatility of flow can be understood by considering a purely advective O_2 transport in a single vessel with a uniform (pulsatile or constant) flow. For this problem, the O_2 concentration at any location x of the vessel is given by $C_T(x,t) = C_T(x_{\text{inlet}}, t - \tau(x))$, where the phase shift $\tau(x)$ is determined by solving $x - x_{\text{inlet}} = \int_0^{\tau(x)} u(t)dt$. As such, the O_2 concentration depends only on the integral of the flow velocity and is not affected much by the flow pulsatility. We also note that the pulsatile amplitude of the pre-capillary (arterial) O_2 concentration as well as its phase difference relative to the cardiac cycle does not affect the model predictions of O_2-related quantities (See Fig. D.7 in the Appendix D). Additionally, the mean amplitude of pO_2 across the capillary network is approximately 2.5% of the inlet pO_2 (SD = 8.6%; Table 2). This reduction in O_2 concentration pulsatility away from the pre-capillaries (inlets) is expected, as diffusion attenuates O_2 pulsatility (see Fig. 3b). These findings imply that it is appropriate to ignore the pulsatility of flow and pressure when estimating O_2-related quantities in the model.

The computational modeling framework developed in this study integrates hemodynamics with the transport of O_2 in/across a coronary capillary network and the consumption of O_2 by the surrounding tissue. Hemodynamics in the capillary network is simulated using a 0-D nonlinear lumped parameter model [13], whereas O_2 transport and consumption are described using a 1-D finite element model that was numerically validated against analytical solutions (Fig. 3). Model predictions of O_2 related metrics in the capillary network are in close agreement with measurements. Specifically, the predicted tissue pO_2 (10.1 ± 3.9 mmHg) and post-capillary venous pO_2 (19.5 ±

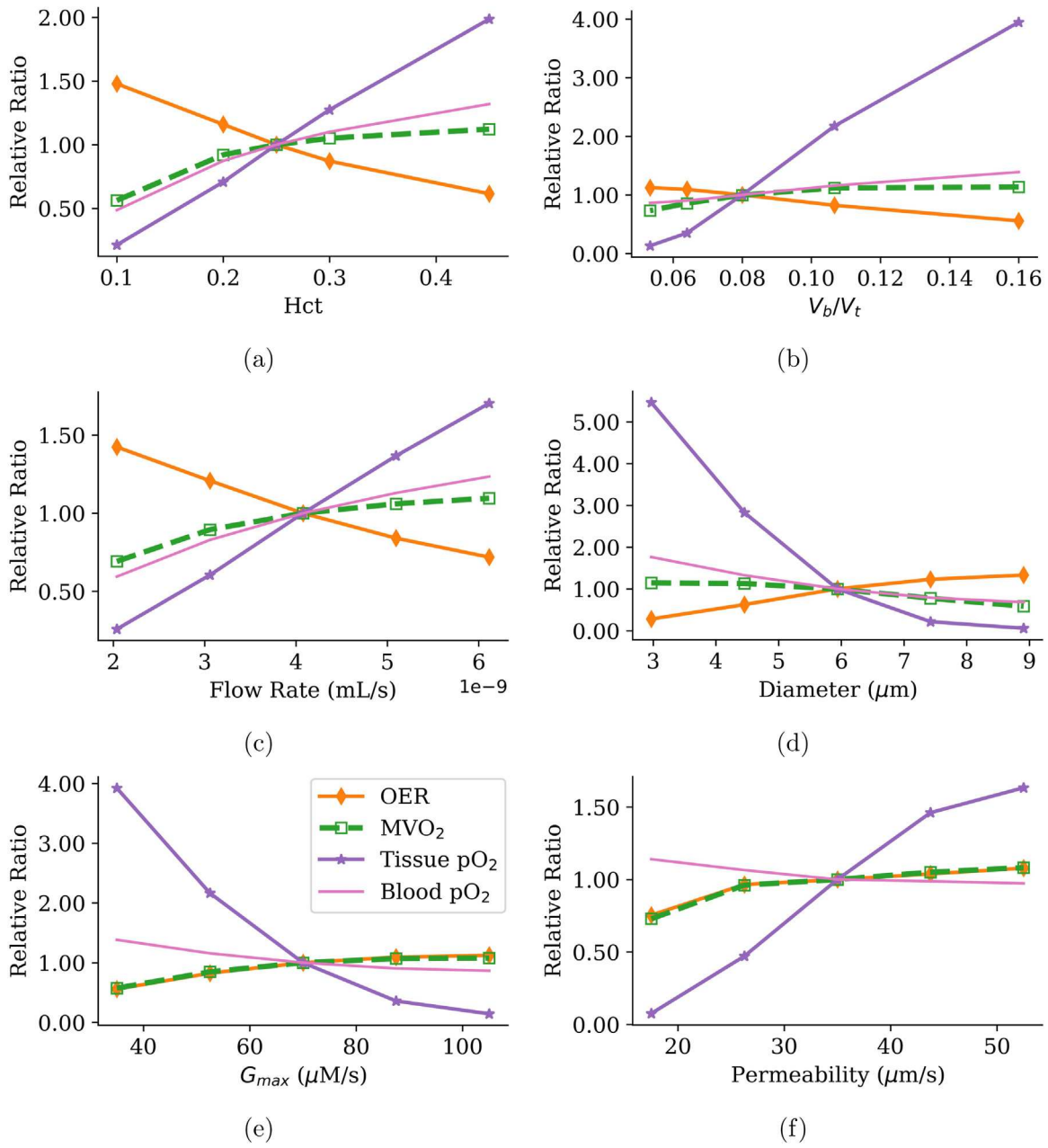

Fig. 4. Sensitivity Analysis. Changes in O_2 extraction ratio (OER), MVO_2 (identical to O_2 extraction rate by tissues), tissue pO_2, and blood pO_2 with respect to changes in (a) hematocrit (H_{ct}), (b) vascular volume fraction (V_b/V_t), (c) flow rate (Q), (d) vessel diameter (D), (e) maximum oxygen consumption rate (G_{max}), and (f) capillary wall permeability (κ_w) at steady-state in the capillary network. "Relative Ratio" represents that these oxygen-related metrics are rescaled and presented as dimensionless ratios relative to their baseline values in a control case. In the control case, the parameters are as follows: OER is 66%, MVO_2 is 8.2 mL O_2/min/100 mL tissue, blood pO_2 is 32 ± 12 mmHg, and tissue pO_2 is 11 ± 10 mmHg.

6.4 mmHg) are within measured values in the myocardial tissue (~7 to 23 mmHg) [40–42] and the coronary sinus (~20 mmHg) [43,44], respectively. Predictions of MVO_2 (equivalent to O_2 extraction) (7.8 ± 1.1 mL O_2/min/100 mL tissue) and OER ($67 \pm 15\%$) are also in agreement with measurements of MVO_2 (~8.8 mL O_2/min/100 mL tissue) [37,41,45] and OER ($\sim 67 \pm 12\%$ from porcine studies) [46].

Sensitivity analyses conducted on the model reveal the effects of various physiological parameters on oxygen levels in the blood and tissues. The pO_2 levels in both blood and tissue are positively correlated with increases in hematocrit H_{ct}, vascular volume fraction V_b/V_t, and flow rate Q (Fig. 4a,b,c), which implies that an increase in these quantities enhance the oxygen transport capacity and delivery. This result is expected because of an increase in these quantities is associated with an increase in red blood cells. Without an increase in the tissue's maximum rate of oxygen consumption G_{max}, however, OER decreases because the O_2 supply rate surpasses the consumption rate (Fig. 4a,b,c). Interestingly, the model predicts a reduction in the O_2 extraction rate when blood flow rate is reduced (Fig. 4c). While this result may appear to be counter-intuitive as one may expect myocardial cells to have more time to extract more oxygen when blood passes the capillary network slowly, the key reason for this behavior is the reduction in the tissue pO_2 (i.e., decreased O_2 availability) as shown in Fig. 4c.

The sensitivity analyses also show that the pO_2 levels are inversely related to the vessel diameter (D) (Fig. 4d) because a larger diameter D corresponds to a larger surface area that facilitates diffusion across vessel walls. On the other hand, the pO_2 levels in the tissue and blood are also inversely related to the maximum rate of oxygen consumption G_{max}

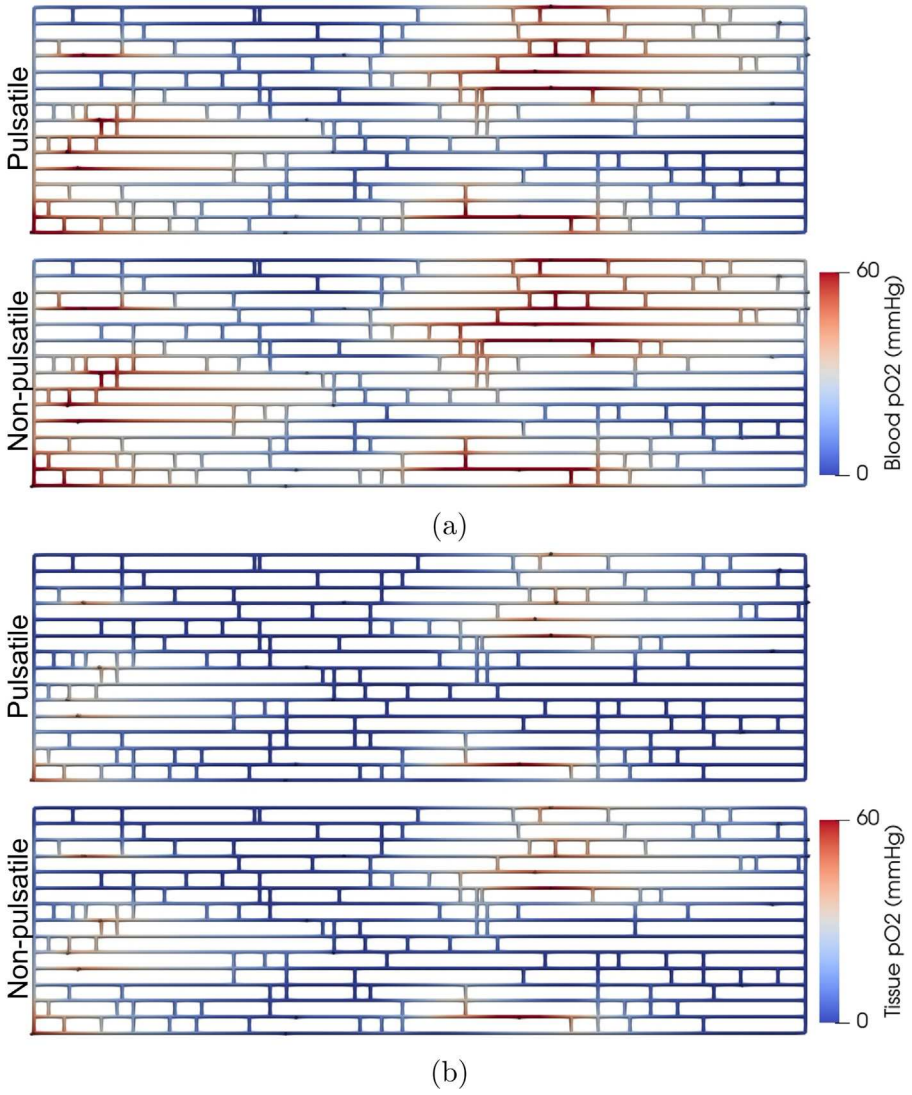

Fig. 5. Pulsatile vs. Non-pulsatile Simulations. Comparisons of pO_2 distribution in (a) blood and (b) tissue with pulsatile and non-pulsatile perfusion in a representative case with the mean inlet, outlet, and intra-myocardial pressures applied to the inlets, outlets, and vessel walls of the capillary network being 40 mmHg, 20 mmHg, and 20 mmHg, respectively. The snapshot for the pulsatile perfusion is taken at $t = 1.2$ s when the inlet pO_2 is 95 mmHg as shown in Fig. 2d. The temporal variation in the spatial distribution of pO_2 within the network is visually indistinguishable, due to the small pulsatile variation in the inlet pO_2, which is especially minimal compared to the large difference between pre-capillary and post-capillary pO_2 (~10 mmHg vs. ~80 mmHg). We also note that diffusion tends to diminish the amplitude of the concentration pulse.

(Fig. 4e), which is associated with a higher metabolic activity (e.g., during exercise and cardiac hypertrophy) [37,45]. Correspondingly, this leads to faster depletion and extraction of oxygen that reduces pO_2 levels and increases OER. Capillary vessel wall permeability κ_w, which can be increased in diabetes [47,48], produces different effects on the pO_2 levels in the tissue and blood (Fig. 4f). Higher permeability allows for more transvascular fluid exchange, enhancing the transfer of O_2 into the tissues. This reduces blood pO_2 and increases tissue pO_2. This effect is particularly pronounced when the tissue's capacity for O_2 consumption has reached its limit; under such conditions, additional O_2 diffusing into the tissue accumulates, thereby increasing the tissue pO_2, as shown in Fig. 4f. Correspondingly, the OER is increased with an increase in κ_w due to enhanced O_2 extraction (Fig. 4f).

This computational modeling framework also serves as a foundation for future patient-specific studies. By incorporating patient-specific data such as coronary vasculature data at medical imaging resolution (capillaries can be extrapolated based on branching pattern rules), arterial pO_2, and venous pO_2, the model can be calibrated further, and then applied to predict individualized effects of heart diseases (e.g., myocardial ischemia/infarction) and treatments (e.g., coronary venous retro-perfusion or reperfusion) on the microvasculature hemodynamics and tissue oxygenation, which are difficult to measure in vivo.

Limitations

The computational modeling framework has several limitations. *First,* the model does not consider O_2 advection within myocardial tissue and diffusion across the tissue volume perpendicular to the vessel axis, which may affect the spatial distribution of tissue pO_2. *Second,* we do not consider the effects of O_2 concentration on hemodynamics. Under specific pathological conditions (e.g., ischemia) where O_2 concentration and hypoxia can become major drivers of blood flow regulation, the regulatory mechanisms may be altered to prioritize O_2 delivery to critically affected tissues. In general, however, O_2 is typically not the primary determinant of blood flow. Rather, blood flow is primarily regulated by factors like vascular tone, autoregulation, neural control, and metabolic demand, as discussed in [49]. *Third,* we apply a no-flux boundary condition at each outlet of the capillary network to simplify the model. While this simplification can produce pO_2 level at the outlets that are comparable to those measured in the

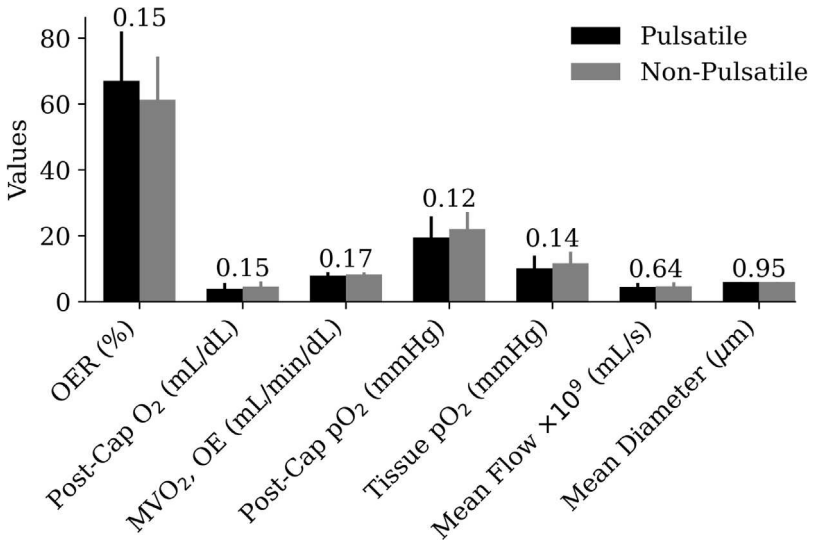

Fig. 6. Pulsatile vs. Non-pulsatile Simulations. Comparisons of oxygen-related metrics between the cases with pulsatile and non-pulsatile perfusion, where the vertical lines on the bars represent the standard deviations over all simulations (27 simulations for each of the pulsatile and non-pulsatile perfusion groups) and the p-values from a two-tailed t-test are shown above the vertical lines. In the non-pulsatile group, the average OER over all cases is 8.6% smaller than that in the pulsatile group, and the post-capillary O_2 content (units: mL O_2/dL blood), MVO_2 (in equilibrium with O_2 extraction, OE) (units: mL O_2/min/dL tissue), post-capillary venous pO_2, tissue pO_2, time-average flow rate and vessel diameter over a cardiac cycle are 17.5%, 4.4%, 13.2%, 19%, 3.6% and 0.02% higher, respectively, than those in the pulsatile group. The input pre-capillary O_2 content is 11.9 mL O_2/dL blood in all cases. The one-tailed p-values, which can be directly obtained by halving the corresponding two-tailed p-values since the directionality supported by the data, are all greater than 0.05.

veins, it may not apply in some scenarios such as coronary venous retroperfusion, where oxygen dynamics at the venous end might be significantly altered. *Fourth,* although model parameters were derived from measurements and previous studies, which in principle reduces the uncertainty in the model parameters, measurement errors and inter-individual variability may still influence the results. Uncertainty analysis can help refine the model parameters.

5. Summary

In summary, we developed a computational modeling framework that integrates coronary capillary flow with the transport of O_2 in and across the capillary network. The model predictions agree with analytical solutions and experimental measurements. Compared to existing models, this modeling framework is more generic as it can be applied to both steady-state and time-dependent problems. We show that there is no significant difference in the model predictions of O_2-related metrics between cases where pulsatile behaviors (of the flow and O_2) are considered and cases when the pulsatile behaviors are neglected. This finding implies that it is reasonable to neglect the pulsatile behavior when analyzing O_2 transport in the coronary capillary network.

CRediT authorship contribution statement

Haifeng Wang: Writing – original draft, Writing – review & editing, Visualization, Validation, Software, Methodology, Investigation, Formal analysis, Data curation, Conceptualization. **Jenny S. Choy:** Writing – review & editing, Conceptualization. **Ghassan S. Kassab:** Writing – review & editing, Supervision, Project administration, Funding acquisition, Conceptualization. **Lik-Chuan Lee:** Writing – review & editing, Supervision, Project administration, Funding acquisition, Conceptualization.

Declaration of competing interest

The authors declare that they have no known competing financial interests or personal relationships that could have appeared to influence the work reported in this paper.

Acknowledgments

This work was supported by the National Institutes of Health, USA (R01 HL160997) and National Science Foundation, USA (NSF 2222066).

Appendix A. Generalized network formulation

The microcirculation network is described by a system of nonlinear ODEs obtained from invoking mass conservations in each vessel i with flow Q_i (Eq. (2)) and at each junction point, i.e.,

$$\sum_{i=1}^{k} Q_i = 0, \tag{A.16}$$

where k is the total number of vessels connected to the junction. We solve the coronary network flow based on mass conservations at each vessel midpoint (Eq. (2)) and at each vessel's nodal junction (Eq. (A.16)). Under the assumption that $\frac{dC^i}{dt} = 0$, Eq. (2) can be rearranged as:

$$\frac{dP^i_{\text{mid}}}{dt} = \frac{2G^i}{C^i}(P^i_{\text{in}} + P^i_{\text{out}} - 2P^i_{\text{mid}}) + \frac{dP^i_T}{dt}, \tag{A.17}$$

where $G^i = \frac{1}{R^i_1} = \frac{1}{R^i_2}$. The mass conservation at the inlet node of a vessel i connected to k vessels yields:

$$(P^i_{\text{mid}} - P^i_{\text{in}})G^i + \sum_{j=1}^{k}(P^j_{\text{mid}} - P^i_{\text{in}})G^j = 0, \tag{A.18}$$

i.e.,

$$P^i_{\text{in}} = \frac{P^i_{\text{mid}}G^i + \sum_{j=1}^{k} P^j_{\text{mid}}G^j}{G^i + \sum_{j=1}^{k} G^j}. \tag{A.19}$$

Similarly, applying mass balance at the outlet node of the vessel i connected to m vessels (where m is not necessarily equal to k) gives:

$$P^i_{\text{out}} = \frac{P^i_{\text{mid}}G^i + \sum_{l=1}^{m} P^l_{\text{mid}}G^l}{G^i + \sum_{l=1}^{m} G^l}. \tag{A.20}$$

Eventually, by inserting Eqs. (A.18) and (A.19) into Eq. (A.17), we obtain a system of N nonlinear ODEs for an arbitrary network

consisting of N vessels in total. The N nonlinear ODEs describing the intravascular pressure at the midpoint of each vessel based on the pressures in its corresponding neighbors can be expressed in matrix form as:

$$\frac{d\mathbf{P}_{\text{mid}}}{dt} = \mathbf{A}\mathbf{P}_{\text{mid}} + \mathbf{B}. \tag{A.21}$$

Appendix B. Weak forms of the 1-D oxygen transport model

B.1. Blood domain

Eq. (7) can be rewritten as:

$$\frac{dC_T}{dt} + \mathcal{L}(C_T, C_F) = S, \tag{B.22}$$

where $S = \sigma C_F^t$, $\sigma = \frac{\kappa_w A}{V_b}$, and

$$\mathcal{L}(C_T, C_F) = U\frac{dC_T}{dx} - D_F\frac{d^2C_F}{dx^2} + \sigma C_F. \tag{B.23}$$

Note that C_T is a function of C_F.

Using the fourth-order Padé approximation for the time discretization, Eq. (B.22) can be rewritten as:

$$\frac{dC_T}{dt} + W\left(\mathcal{L}(\Delta C_T, \Delta C_F) - \Delta S\right) = w\left(S^n - \mathcal{L}(C_T^n, C_F^n)\right), \tag{B.24}$$

where

$$\Delta C_T = \begin{pmatrix} C_T^{n+1/2} - C_T^n \\ C_T^{n+1} - C_T^{n+1/2} \end{pmatrix}, \tag{B.25}$$

$C_T^{n+1/2} = (C_T^{n+1} + C_T^n)/2$, and this also applies to ΔC_F and ΔS.

$$W = \frac{1}{24}\begin{pmatrix} 7 & -1 \\ 13 & 5 \end{pmatrix}. \tag{B.26}$$

$$w = \begin{pmatrix} 0.5 \\ 0.5 \end{pmatrix}. \tag{B.27}$$

Note that C_T^n and C_F^n are from the previous time step. The residual term is:

$$\mathcal{R}(\Delta C_T, \Delta C_F) = \frac{dC_T}{dt} + W\left(\mathcal{L}(\Delta C_T, \Delta C_F) - \Delta S\right) - w\left(S^n - \mathcal{L}(C_T^n, C_F^n)\right). \tag{B.28}$$

Finally, the consistently stabilized weak form of the problem is given by:

$$(\omega, \frac{dC_T}{dt}) + (\omega, W\left(\mathcal{L}(\Delta C_T, \Delta C_F) - \Delta S\right)) - (\omega, w\left(S^n - \mathcal{L}(C_T^n, C_F^n)\right)) + \sum_e (\tau\mathcal{P}(\omega), \mathcal{R}(\Delta C_T, \Delta C_F)) = 0, \tag{B.29}$$

where the intrinsic time scale matrix is:

$$\tau = \left[\frac{W^{-1}}{\Delta t} + \left(\frac{2U}{h} + \frac{4D_F}{h^2} + \sigma\right) I\right]^{-T} W^{-1}, \tag{B.30}$$

and the $\mathcal{P}$ operator characterizes the stabilization technique. For SUPG, $\mathcal{P} = WU\nabla\omega$. The stabilization terms, $\sum_e(\tau\mathcal{P}(\omega), \mathcal{R}(\Delta C_T, \Delta C_F))$, spans all finite elements.

B.2. Tissue domain

When considering diffusion in tissue:

$$F_{n+1}^t(C_F^t; C_F; v) = \int_\Omega \frac{C_F^t - C_F^{t,n}}{\Delta t} v dx - \int_\Omega \frac{\kappa_w A}{V_t}(C_F - C_F^t) v dx + \int_\Omega \text{MVO}_2\, v dx + \int_\Omega D_F \frac{dC_F^t}{dx}\frac{dv}{dx} dx + \int_\Omega D_{Mb} C_{Mb} \frac{d(C_F^t/(C_F^t + C_{50}))}{dx}\frac{dv}{dx} dx. \tag{B.31}$$

Eq. (10) can be also rewritten in a form as Eq. (B.22), where

$$\mathcal{L}(C_F^t) = \frac{\kappa_w A}{V_t} C_F^t + \text{MVO}_2(C_F^t) - D_F\frac{d^2C_F^t}{dx^2} - D_{Mb}C_{Mb}\frac{d^2 S_{Mb}(C_F^t)}{dx^2}, \tag{B.32}$$

and $S^t = \frac{\kappa_w A}{V_t} C_F$. Using the fourth-order Padé approximation for the time discretization, the weak form of the problem shown in Eq. (B.31) is given by:

$$(\omega, \frac{dC_F^t}{dt}) + (\omega, W\left(\mathcal{L}(\Delta C_F^t) - \Delta S^t\right)) - (\omega, w\left(S^{t,n} - \mathcal{L}(C_F^{t,n})\right)) = 0. \tag{B.33}$$

Appendix C. Analytical solutions for benchmark tests

For an 'advection + diffusion' problem given by:

$$\frac{dC_F(x,t)}{dt} = -U\frac{dC_F(x,t)}{dx} + D_F\frac{d^2C_F(x,t)}{dx^2}, \tag{C.34}$$

with the boundary conditions of $C_F(0,t) = 0$ and $C_F(L,t) = 0$, and the initial condition

$$C_F(x,0) = C_0 e^{-\left(\frac{x-x_0}{l_c}\right)^2}, \tag{C.35}$$

where C_0 is prescribed and equal to αpO_2 with $\text{pO}_2 = 95\,\text{mmHg}$ and $\alpha = 1.35\times10^{-12}\,\text{mol/(mm}^3\,\text{mmHg)}$, $x_0 = 0.3L$, and the characteristic length $l_c = 0.03L$, the exact solution is:

$$C_F(x,t) = \frac{C_0}{\sqrt{1 + 4D_F t/l_c^2}} e^{-\left(\frac{x - x_0 - Ut}{l_c\sqrt{1+4D_F t/l_c^2}}\right)^2}. \tag{C.36}$$

The permeation problem of O_2 flux across the vessel wall is validated by uniformly initializing the vessel pO_2 at 95 mmHg, i.e., $C_F^0 = C_F(t=0) = 95\,\text{mmHg}/\alpha$. The initial tissue pO_2 is set to 0 mmHg, and the tissue oxygen consumption to 0. Then, we have:

$$\frac{dC_F(x,t)}{dt} = -\frac{\kappa_w A}{V_b}(C_F - C_F^t), \tag{C.37}$$

$$\frac{dC_F^t(x,t)}{dt} = \frac{\kappa_w A}{V_t}(C_F - C_F^t). \tag{C.38}$$

For easier understanding, Eqs. (C.37) and (C.38) can be rewritten as:

$$\frac{dC_F(x,t)}{dt}V_b = JA,\ \ \frac{dC_F^t(x,t)}{dt}V_t = -JA,\ \ J = -\kappa_w(C_F - C_F^t). \tag{C.39}$$

When $V_t = V_b$, these two equation can be rewritten as:

$$\frac{dC_F^t(x,t)}{dt} - \frac{dC_F(x,t)}{dt} = 2\frac{\kappa_w A}{V_t}(C_F - C_F^t). \tag{C.40}$$

The analytical solutions are:

$$C_F(t) = \frac{C_F^0}{2}\left(1 + e^{-2\frac{\kappa_w A}{V_t}t}\right), \tag{C.41}$$

and

$$C_F^t(t) = \frac{C_F^0}{2}\left(1 - e^{-2\frac{\kappa_w A}{V_t}t}\right). \tag{C.42}$$

Appendix D. Supplementary results

Fig. D.1 shows the comparison between cases with and without considering O_2 diffusion in surrounding tissues along the direction parallel to the vessel axis. It is evident that accounting for O_2 diffusion within surrounding tissues helps prevent unrealistic sharp changes in O_2 content in the tissues.

Fig. D.2 shows the visualization of the relationship between S_{Hb} and blood pO_2, as well as between MVO_2 and tissue pO_2.

Fig. D.4 shows that large Courant–Friedrichs–Lewy (CFL) numbers, particularly when CFL > 0.5, lead to non-negligible numerical errors.

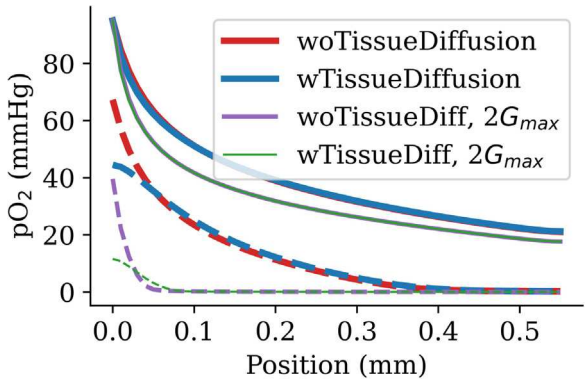

Fig. D.1. Comparison between cases with and without considering O_2 diffusion in tissues using a single vessel. The vessel diameter and length are $D = 6$ μm and $L = 550$ μm, respectively. The flow rate is $Q = 3.6 \times 10^{-9}$ mL/s. The maximum O_2 consumption rate is $G_{max} = 70$ μM/s. Dashed lines show tissue pO_2 and continuous lines for blood pO_2. woTissueDiff, without considering O_2 diffusion in surrounding tissues; wTissueDiff, with considering O_2 diffusion in surrounding tissues.

To prevent numerical instability and ensure the prediction accuracy, a CFL value of 0.1 is recommended.

Fig. D.7a shows that the pulsatile amplitude (pulsatility) of the pre-capillary (arterial) O_2 concentration does not affect the model predictions of the O_2-related quantities. For example, the OER is 78.93, 78.94, and 78.99 in cases where the amplitudes of pre-capillary pO_2 are 0 mmHg, 10 mmHg, and 30 mmHg, respectively. Fig. D.7b shows that the O_2-related quantities are also not sensitive to the phase difference between the respiratory cycle and the cardiac cycle, as well as to the ratio between the respiratory and heart rates, even when the ratio is non-integer.

Data availability

All data generated or analyzed during this study are included in the article/appendix. Further inquiries can be directed to the corresponding author/s.

References

[1] P. Dominelli, C. Wiggins, T. Roy, T. Secomb, T. Curry, M. Joyner, The oxygen cascade during exercise in health and disease, Mayo Clin. Proc. 96 (4) (2021) 1017–1032.
[2] D. Poole, D. Hirai, S. Copp, T. Musch, Muscle oxygen transport and utilization in heart failure: implications for exercise (in)tolerance, Am. J. Physiol. Heart Circ. Physiol. 302 (5) (2012) H1050–63.
[3] T. Wang, A. Sánchez-Nadales, E. Igbinomwanhia, P. Cremer, B. Griffin, B. Xu, Diagnosis of infective endocarditis by subtype using 18F-fluorodeoxyglucose positron emission tomography/computed tomography: A contemporary meta-analysis, Circ. Cardiovasc. Imaging 13 (6) (2020) e010600.
[4] M. Dewey, M. Siebes, M. Kachelrieß, K. Kofoed, P. Maurovich-Horvat, K. Nikolaou, W. Bai, A. Kofler, R. Manka, S. Kozerke, A. Chiribiri, T. Schaeffter, F. Michallek, F. Bengel, S. Nekolla, P. Knaapen, M. Lubberink, R. Senior, M. Tang, J. Piek, T. van de Hoef, J. Martens, L. Schreiber, Clinical quantitative cardiac imaging for the assessment of myocardial ischaemia, Nat. Rev. Cardiol. 17 (5) (2020) 427–450.
[5] A. Popel, Theory of oxygen transport to tissue, Crit. Rev. Biomed. Eng. 17 (3) (1989) 257–321.
[6] D. Beard, J. Bassingthwaighte, Modeling advection and diffusion of oxygen in complex vascular networks, Ann. Biomed. Eng. 29 (4) (2001) 298–310.
[7] Q. Fang, S. Sakadzić, L. Ruvinskaya, A. Devor, A. Dale, D. Boas, Oxygen advection and diffusion in a three-dimensional vascular anatomical network, Opt. Express 16 (22) (2008) 17530–17541.
[8] T.W. Secomb, Chapter 15 - simulation of blood flow and oxygen transport in vascular networks, in: Z.S. Galis (Ed.), The Vasculome, Academic Press, 2022, pp. 173–179.
[9] D. Beard, J. Bassingthwaighte, Advection and diffusion of substances in biological tissues with complex vascular networks, Ann. Biomed. Eng. 28 (3) (2000) 253–268.
[10] D. Beard, Computational framework for generating transport models from databases of microvascular anatomy, Ann. Biomed. Eng. 29 (10) (2001) 837–843.
[11] D. Beard, Modeling of oxygen transport and cellular energetics explains observations on in vivo cardiac energy metabolism, PLoS Comput. Biol. 2 (9) (2006) e107.
[12] G. Liu, A. Qutub, P. Vempati, F. Mac Gabhann, A. Popel, Module-based multiscale simulation of angiogenesis in skeletal muscle, Theor. Biol. Med. Model. 8 (6) (2011) 1–26.
[13] H. Wang, L. Fan, J. Choy, G. Kassab, L. Lee, Simulation of coronary capillary transit time based on full vascular model of the heart, Comput. Methods Programs Biomed. 243 (2024) 107908.
[14] H. Wang, L. Fan, J. Choy, G. Kassab, L. Lee, Mechanisms of coronary sinus reducer for treatment of myocardial ischemia: in silico study, J. Appl. Physiol. (1985) 136 (5) (2024) 1157–1169.
[15] J. Choy, T. Hubbard, H. Wang, Y. Awakeem, P. Khosravi, B. Khadivi, J. Navia, G. Stone, L. Lee, G. Kassab, Preconditioning with selective autoretroperfusion: In vivo and in silico evidence of washout hypothesis, Front. Bioeng. Biotechnol. 12 (2024) 1386713.
[16] A. Zingaro, C. Vergara, L. Dede', F. Regazzoni, A. Quarteroni, A comprehensive mathematical model for cardiac perfusion, Sci. Rep. 13 (1) (2023) 14220.
[17] L. Papamanolis, H. Kim, C. Jaquet, M. Sinclair, S. M, I. Danad, P. van Diemen, P. Knaapen, L. Najman, H. Talbot, C. Taylor, I. Vignon-Clementel, Myocardial perfusion simulation for coronary artery disease: A coupled patient-specific multiscale model, Ann. Biomed. Eng. 49 (5) (2021) 1432–1447.
[18] S. Heath Richardson, J. Mackenzie, N. Thekkethil, L. Feng, J. Lee, C. Berry, N.A. Hill, X. Luo, H. Gao, Cardiac perfusion coupled with a structured coronary network tree, Comput. Methods Appl. Mech. Engrg. 428 (2024) 117083.
[19] R. Namani, G. Kassab, Y. Lanir, Integrative model of coronary flow in anatomically based vasculature under myogenic, shear, and metabolic regulation, J. Gen. Physiol. 150 (1) (2018) 145–168.
[20] R. Dash, J. Bassingthwaighte, Simultaneous blood-tissue exchange of oxygen, carbon dioxide, bicarbonate, and hydrogen ion, Ann. Biomed. Eng. 34 (7) (2006) 1129–1148.
[21] W. Federspiel, A. Popel, A theoretical analysis of the effect of the particulate nature of blood on oxygen release in capillaries, Microvasc. Res. 32 (2) (1986) 164–189.
[22] D. Castro, S. Patil, M. Zubair, M. Keenaghan, Arterial Blood Gas, StatPearls [Internet]. Treasure Island (FL): StatPearls Publishing, In, 2024.
[23] F. Formenti, N. Bommakanti, R. Chen, J.N. Cronin, H. McPeak, D. Holopherne-Doran, G. Hedenstierna, C.E.W. Hahn, A. Larsson, A.D. Farmery, Respiratory oscillations in alveolar oxygen tension measured in arterial blood, Sci. Rep. 7 (1) (2017) 7499.
[24] H. Walker, W. Hall, J. Hurst, editors, Clinical Methods: The History, Physical, and Laboratory Examinations, 3rd ed., Butterworths, Butterworth Publishers. Boston, 1990.
[25] J.E. Hall, M.E. Hall, Guyton and Hall Textbook of Medical Physiology, 14th Ed., Elsevier, 2020.
[26] B. Duling, C. Desjardins, Capillary hematokrit – what does it mean? Int. Union Physiol. Sci. 2 (2) (1987) 66–69.
[27] K. Rakusan, N. Cicutti, F. Kolar, Cardiac function, microvascular structure, and capillary hematocrit in hearts of polycythemic rats, Am. J. Physiol. Heart Circ. Physiol. 281 (6) (2001) H2425–31.
[28] D. Lobdell, An invertible simple equation for computation of blood O2 dissociation relations, J. Appl. Physiol. Respir. Environ. Exerc. Physiol. 50 (5) (1981) 971–973.
[29] A. Ihdayhid, T. Fairbairn, G. Gulsin, G. Tzimas, E. Danehy, A. Updegrove, J. Jensen, C. Taylor, J. Bax, S. Sellers, J. Leipsic, B. Nørgaard, Cardiac computed tomography-derived coronary artery volume to myocardial mass, J. Cardiovasc. Comput. Tomogr. 16 (3) (2022) 198–206.
[30] P. Smith, D. Clark, Myocardial capillary density and muscle fibre size in rats born and raised at simulated high altitude, Br. J. Exp. Pathol. 60 (2) (1979) 225–230.
[31] L. Ashley, A determination of the diameters of ventricular myocardial fibers in man and other mammals, Am. J. Anat. 77 (1945) 325–363.
[32] K. Sawada, K. Kawamura, Architecture of myocardial cells in human cardiac ventricles with concentric and eccentric hypertrophy as demonstrated by quantitative scanning electron microscopy, Heart Vessels 479, 129—-142, 6.
[33] L. Opi, Mechanisms of cardiac contraction and relaxation., in: E. Braunwald, D. Zipes, P. Libby (Eds.), Heart Disease: A Textbook of Cardiovascular Medicine, 2001, p. 443.
[34] R. Tracy, G. Sander, Histologically measured cardiomyocyte hypertrophy correlates with body height as strongly as with body mass index, Cardiol. Res. Pract. 2011 (2011) 658958.
[35] C. Basso, K. Michaud, G. d'Amati, J. Banner, J. Lucena, K. Cunningham, O. Leone, A. Vink, A. van der Wal, M. Sheppard, A. for European Cardiovascular Pathology, Cardiac hypertrophy at autopsy, Erratum: Virchows Arch. 479 (1) (2021) 79–94.
[36] G. Kassab, Y. Fung, Topology and dimensions of pig coronary capillary network, Am. J. Physiol.-Heart Circ. Physiol. 267 (1) (1994) H319–H325.
[37] O. AbouEzzeddine, B. Kemp, B. Borlaug, B. Mullan, A. Behfar, S. Pislaru, M. Fudim, M. Redfield, P. Chareonthaitawee, Myocardial energetics in heart failure with preserved ejection fraction, Circ. Heart Fail. 12 (10) (2019) e006240.

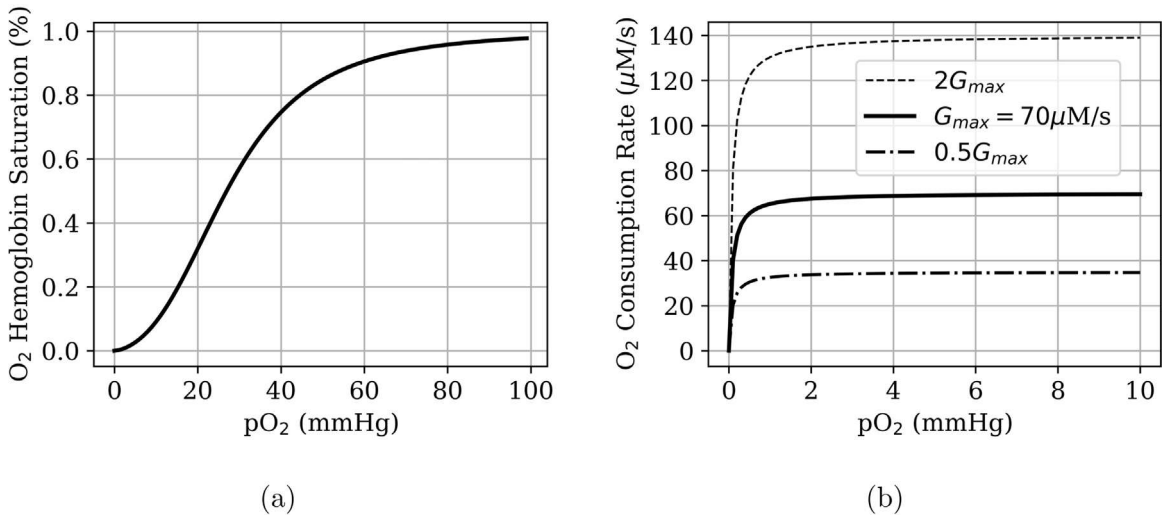

Fig. D.2. (a) The oxygen–hemoglobin dissociation curve, showing the proportion of hemoglobin in its saturated form against the blood oxygen tension; (b) O_2 consumption rate as a function of tissue oxygen tension (Eq. (12)). Note that the oxygen tension pO_2 is related to the free oxygen concentration, C_F, and the solubility coefficient of oxygen, α, by $pO_2 = C_F/\alpha$.

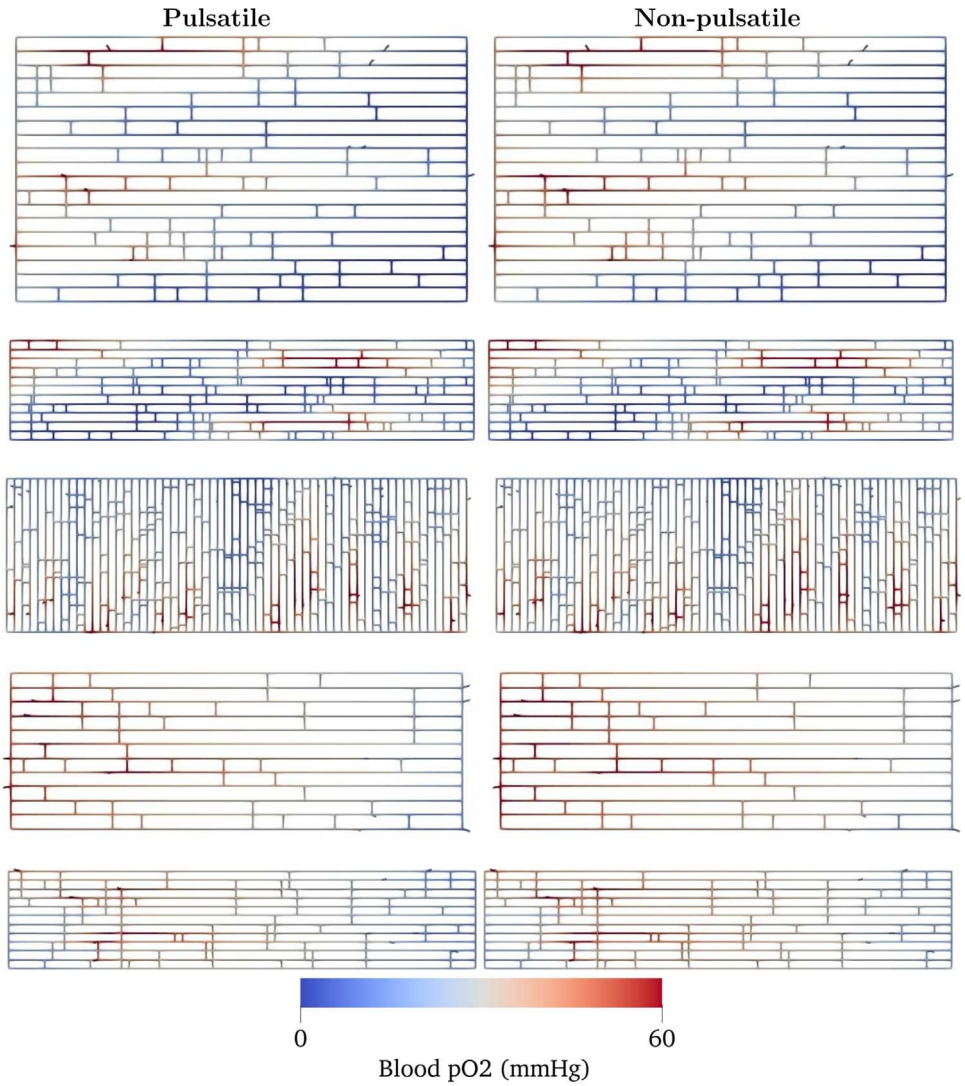

Fig. D.3. Spatial distribution of blood pO_2 in 5 different capillary networks with pulsatile and non-pulsatile perfusion. The mean inlet, outlet, and intra-myocardial pressures applied to the capillary network are 40 mmHg, 20 mmHg, and 20 mmHg, respectively. The input pulsatile waveforms are shown in Fig. 2.

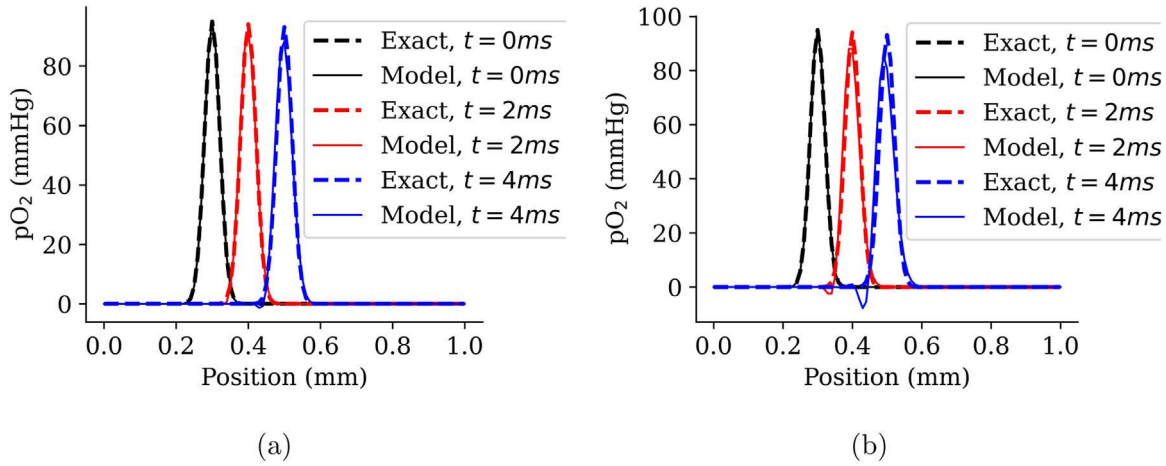

Fig. D.4. Compared to Fig. 3b, only the time step size increased in these 2 cases: (a) CFL = 0.5; (b) CFL = 1. A Courant–Friedrichs–Lewy (CFL) number less than 1.0 is often assured in numerical simulations.

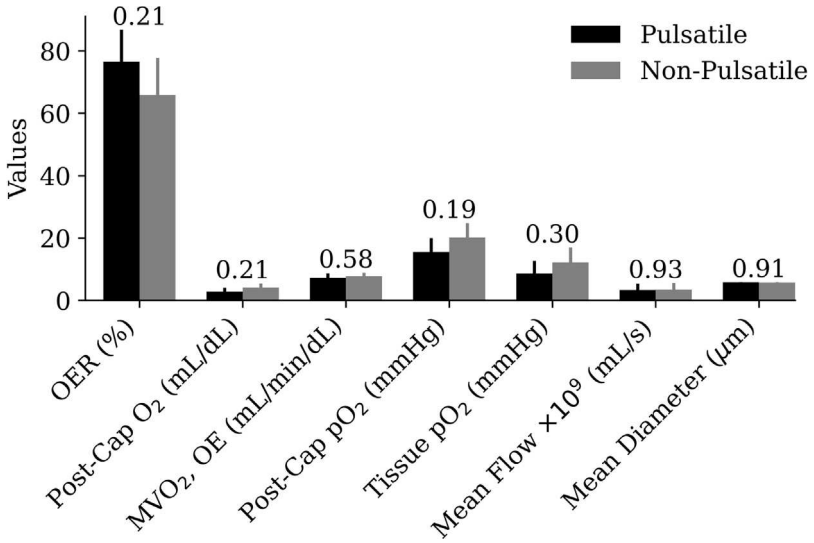

Fig. D.5. Comparisons of oxygen-related metrics between the cases with pulsatile and non-pulsatile perfusion in 6 different capillary networks (as shown in Figs. 5 and D.3), where the vertical lines on the bars represent the standard deviations and the p-values from a two-tailed t-test are shown above the vertical lines. The lowest p-value is 0.19 in the model prediction of post-capillary pO_2.

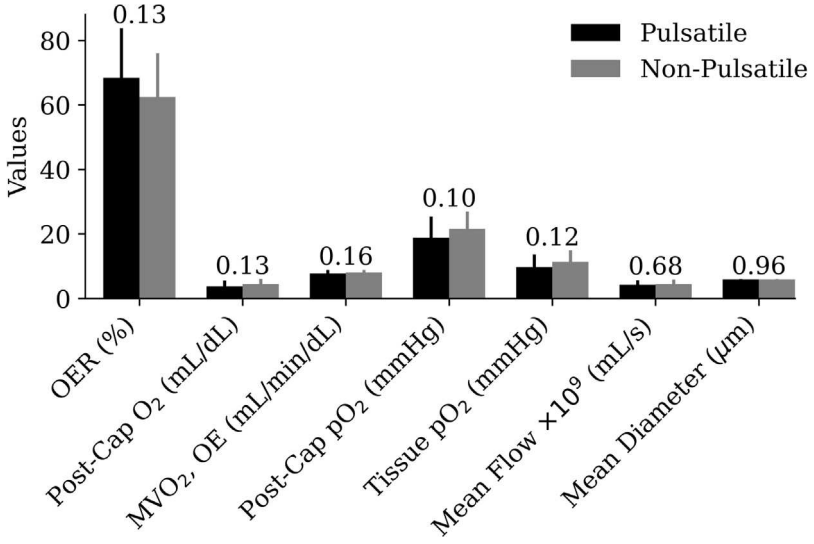

Fig. D.6. Comparisons of oxygen-related metrics between the cases with pulsatile and non-pulsatile perfusion over all simulations (32 simulations for each of the pulsatile and non-pulsatile perfusion groups; Figs. 6 and D.5). The vertical lines on the bars represent the standard deviations and the p-values from a two-tailed t-test are shown above the vertical lines. The lowest p-value is 0.1 in the model prediction of post-capillary pO_2.

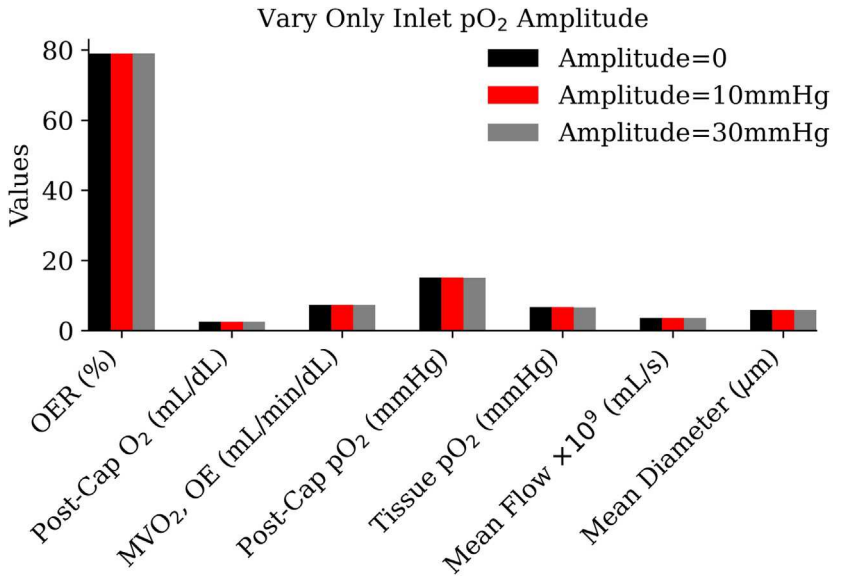

(a)

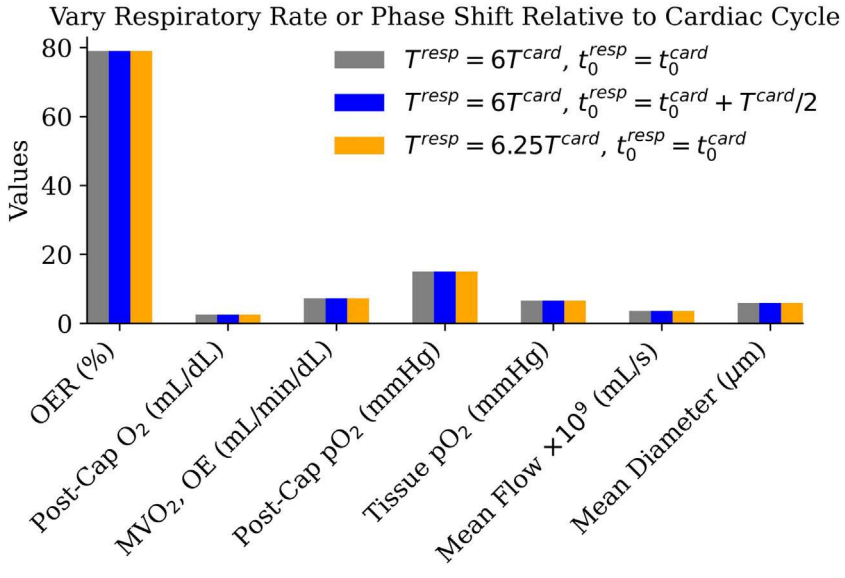

(b)

Fig. D.7. Comparisons of oxygen-related quantities (a) between cases with different pulsatile amplitudes of the pre-capillary inlet pO_2 and (b) between cases with different respiratory rates or phase shifts relative to cardiac cycle. The pulsatile inlet, outlet, and intra-myocardial pressures with the mean values being 40 mmHg, 20 mmHg, and 20 mmHg (Fig. 2), are applied to the inlets, outlets, and vessel walls of the capillary network (Fig. 1), respectively. The mean pre-capillary pO_2 is 95 mmHg in all cases. resp, respiratory; card, cardiac.

[38] P. Salisbury, C. Cross, P. Rieben, Intramyocardial pressure and strength of left ventricular contraction, Circ. Res. 10 (1962) 608–623.

[39] X.G. Sun, R.S. Chen, G.Z. Wang, X.Y. Yang, X.Y. Zhao, J.F. Yu, R. Zhang, Y.P. Ji, J. Li, H. Li, Y. Zhang, M.X. Ma, R. Chen, Y.X. Zou, Ultra-fast response polymer optical fiber oxygen measurement device and its preliminary experimental report on continuous dynamic change of arterial oxygen partial pressure under mechanical ventilation in living animals (in Chinese), Zhongguo Ying Yong Sheng Li Xue Za Zhi 37 (1) (2021) 104–112.

[40] L. Wiener, M. Feola, J.r. Templeton, H. Hamarman, A. Venkataswamy, Monitoring tissue oxygenation of the heart after myocardial revascularization, Am. J. Cardiol. 38 (1) (1976) 38–45.

[41] D. Hauton, A. Al-Shammari, E. Gaffney, S. Egginton, Maternal hypoxia decreases capillary supply and increases metabolic inefficiency leading to divergence in myocardial oxygen supply and demand, PLoS One 10 (6) (2015) e0127424.

[42] M. Oknińska, Z. Zambrowska, K. Zajda, A. Paterek, K. Brodaczewska, U. Mackiewicz, C. Szczylik, A. Torbicki, C. Kieda, M. Maczewski, Right ventricular myocardial oxygen tension is reduced in monocrotaline-induced pulmonary hypertension in the rat and restored by myo-inositol trispyrophosphate, Sci. Rep. 11 (1) (2021) 18002.

[43] P. Zong, J. Tune, H. Downey, Mechanisms of oxygen demand/supply balance in the right ventricle, Exp. Biol. Med. (Maywood) 230 (8) (2005) 507–519.

[44] E. Grossini, F. Prodam, G. Walker, L. Sigaudo, S. Farruggio, K. Bellofatto, P. Marotta, C. Molinari, D. Mary, G. Bona, G. Vacca, Effect of monomeric adiponectin on cardiac function and perfusion in anesthetized pig, J. Endocrinol. 222 (1) (2014) 137–149.

[45] N. Hansson, J. Sörensen, H. Harms, W. Kim, R. Nielsen, L. Tolbod, J. Frøkiær, K. Bouchelouche, K. Dodt, I. Sihm, S. Poulsen, H. Wiggers, Myocardial oxygen consumption and efficiency in aortic valve stenosis patients with and without heart failure, J. Am. Heart Assoc. 6 (2) (2017) e004810.

[46] M. Herbertson, H. Werner, J. Russell, K. Iversen, K. Walley, Myocardial oxygen extraction ratio is decreased during endotoxemia in pigs, J. Appl. Physiol. (1985) 79 (2) (1995) 479–486.

[47] G. Viberti, Increased capillary permeability in diabetes mellitus and its relationship to microvascular angiopathy, Am. J. Med. 75 (5B) (1983) 81–84.

[48] G. Spinetti, N. Kraenkel, C. Emanueli, P. Madeddu, Diabetes and vessel wall remodelling: from mechanistic insights to regenerative therapies, Cardiovasc. Res. 78 (2) (2008) 265–273.

[49] L. Fan, H. Wang, G. Kassab, L. Lee, Review of cardiac-coronary interaction and insights from mathematical modeling, WIREs Mech. Dis. 16 (3) (2024) e1642.